Journal of
MATERIALS RESEARCH

Article
DOI:10.1557/s43578-023-01129-z

Effect of cation insertion on the stability of gliding arc plasma-precipitated mesoporous MnO_2 dye bleaching catalysts

Franck W. Boyom-Tatchemo[1,2,a], **François Devred**[1], **Elie Acayanka**[2],
Georges Kamgang-Youbi[2], **Serge Nzali**[3], **Samuel Laminsi**[2], **Eric M. Gaigneaux**[1,a)]
[1] *Institute of Condensed Matter and Nanosciences (IMCN), Université Catholique de Louvain, Place Louis Pasteur 1, L4.01.09, 1348 Louvain-La-Neuve, Belgium*
[2] *Department of Inorganic Chemistry, University of Yaoundé I, P.O. Box 812, Yaoundé, Cameroon*
[3] *School of Wood, Water and Natural Resources, Faculty of Agronomy and Agricultural Sciences, University of Dschang, P.O. Box 786, Ebolowa, Cameroon*
a) Address all correspondence to these authors. e-mails: boyom.william@yahoo.com; eric.gaigneaux@uclouvain.be

Received: 15 May 2023; accepted: 27 July 2023; published online: 11 August 2023

α-MnO_2 and γ-MnO_2 polymorphs were, respectively, obtained from the plasma precipitation of $KMnO_4$ and $Mn(CH_3COO)_3·2H_2O$ precursors. The obtained powders were calcined at 150 °C, 210 °C and 400 °C, and characterized by X-ray diffraction, Raman spectroscopy, Fourier transform infrared spectroscopy (FTIR), Thermogravimetric analysis (TGA), X-ray photoelectron spectroscopy (XPS), nitrogen physisorption and Scanning electron microscopy (SEM). As a result, the calcination does not significantly affect textural properties and crystalline structure of the α-MnO_2, while γ-MnO_2 is transformed into β-MnO_2 for temperatures above 400 °C. The thermal stability α-MnO_2 is due to the K^+ ions insertion in its 4.6 Å × 4.6 Å tunnels and corroborated the catalytic performance of 100, 98, 98 and 97% compared to 71, 54, 52 and 48% for γ-MnO_2 after four successive reuse cycles on Tartrazine Yellow dye. The insertion of cationic species (K^+, Na^+, Mg^{2+}) into the structure of MnO_2 reinforces its crystalline structure and promotes the formation of powerful oxidizing species through oxygen vacant sites.

Introduction

In recent decades, a great interest in the synthesis and use of metal oxides nanoparticles has developed, and therefore, fundamental and applied research is now focused on this topic. The synthesis of mesoporous nanomaterials and, particularly, the synthesis of transition metal oxides with high stability, attract the interest of many researchers, intending to improve their industrial applications [1, 2]. Furthermore, the environmental impact of wastewater coming from various industrial activities has been the target of recent developments in heterogeneous catalysis [3–6]. This is why several recent works have focused on the development of nanostructures based on metal oxides as a hetero-catalyst to improve industrial processing units [2, 7–9]. Among them, MnO_2 based on the wide variety of its polymorphs is a compelling material because of its interesting applications being used as a sensor, in energy storage and catalysis, where it exhibited relatively high catalytic activity in the decomposition of organic compounds by oxidation. Moreover, its low production cost compared to noble metals in particular and its environmental friendliness are very appealing [10, 11]. Various types of MnO_2 nanostructures were prepared through sol–gel [12], co-precipitation [13], thermal decomposition [14], and hydrothermal processes [15–17]. However, these methods require long preparation times, rough synthesis conditions, and, in some cases, the use of surfactants. Therefore, gliding arc plasma appears as an innovative route, more ecological than classical chemistry one, for nanomaterials synthesis either through oxidizing (HO·) or reducing (NO·) species generated in plasma conditions [18, 19]. Boyom et *al.* reported that various polymorphs of MnO_2 with different morphologies could successfully be synthesized via the reduction of $KMnO_4$ (Mn^{7+}) or the oxidation of $Mn(CH_3COO)_3·2H_2O$ (Mn^{3+}) solutions by changing plasma parameters such as voltage or airflow [19, 20]. It appears that this synthesis route creates powders that show mesoporosity, making that it then became interesting to test them as heterogeneous catalysis in advanced oxidation processes (AOPs). Now, the question is to know if this process could prepare MnO_2 (Mn^{4+}) mesoporous materials with stable physicochemical properties along heating, and that remain catalytically stable during their use. Knowing that some catalytic reactions (most in gas phase) are performed under heating, the present work consists firstly, to study the impact of the calcination temperature on the properties of α-MnO_2 and γ-MnO_2 obtained, respectively, via the plasma-reduction of $KMnO_4$ and the oxidation of $Mn(CH_3COO)_3{\cdot}2H_2O$. Secondly, to evaluate the crystalline structure, textural and morphological stabilities along the catalytic bleaching of Tartrazine Yellow, chosen as a model pollutant, and their reuse for successive catalytic cycles. Due to its many advantages such as its easy recovery and its possible regeneration and reuse, MnO_2 has indeed been widely employed as a heterogeneous catalyst in advanced oxidation processes (AOPs) for depollution purposes [21–24]. Gong et *al.* showed that MnO_2 nanorods supported on mesoporous silica could be successfully used for 6 cycles of bleaching/degradation of Rhodamine B [25]. In particular, we assess here the effect of the cation insertion that occurs within the MnO_2 structure during its synthesis via gliding arc plasma, on its thermal stability and catalytic reuse.

Results and discussion

Effect of calcination on the properties of plasma-precipitated MnO_2

Structural analyses

Figure 1 depicts the XRD patterns of both fresh plasma-precipitated and calcined materials at 150 °C, 210 °C, and 400 °C for 3 h. The calcined material obtained via plasmachemical reduction of $KMnO_4$ at different temperatures [Fig. 1(a)], shows peaks at 12.8°, 18.1°, 28.4°, 37.5°, 42.1°, 50°, 56.3°, 60.2°, 65.5°, 68° and 72.3°, which correspond to the α-MnO_2 polymorph (JCPDS 44-0141) [26, 27]. We observed that the crystalline structure of α-MnO_2 remained stable after calcination up to 400 °C, which could be ascribed to its structure consolidation thanks to the presence of K^+ within the 4.6 Å × 4.6 Å tunnels that form this polymorph [28, 29]. Sinha et al. showed that the crystalline structure of α-MnO_2 nanowires prepared by reduction of $KMnO_4$ remains stable until 400 °C of calcination [30]. Meanwhile, the material obtained by plasmachemical oxidation of $Mn(CH_3COO)_3.2H_2O$ [Fig. 1(b)], displayed diffraction peaks at 22.2°, 34.9°, 36.8°, 38.5°, 42.4°, 56.2°, 62.6°, 65.4° and 68.7°, indexed to γ-MnO_2 (JCPDS 14–0644) [31]. These peaks remain unchanged after calcinations at 150 °C and 210 °C, but were shifted to 28.6°, 37.5°, 41.1, 42.8°, 46.2°, 56.6°, 59.2°, 65°, 67° and 72.8° after calcination at 400 °C [Fig. 1(b)], which correspond to the β-MnO_2 polymorph (JCPDS 24-0735) [32–34] corroborating the previous author's works [35]. Hence, plasma-precipitated α-MnO_2 reveals higher crystalline stability than γ-MnO_2, which could be due to the nature of the species within the tunnels that form the respective polymorphs.

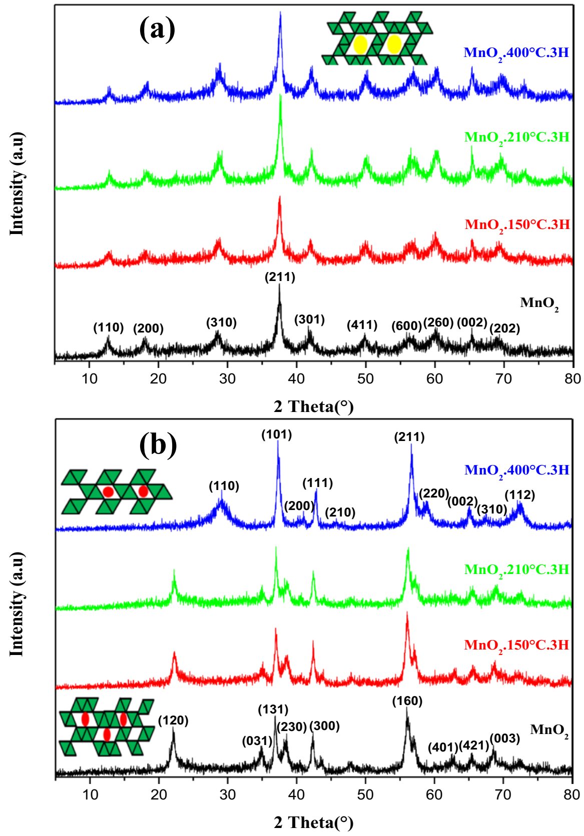

Figure 1: XRD patterns of plasma-precipitated MnO_2 material obtained from (a) $KMnO_4$ precursor, as such (black curve) and after calcination at 150 (red), 210 (green) and 400 °C (blue), and (b) $Mn(CH_3COO)_3.2H_2O$, as such and after calcination at different temperatures (same sequence of color curves). On (a) panel, indexation of the peaks is done from α-MnO_2 polymorph card (JCPDS 44-0141), on (b) panel indexation is made from γ-MnO_2 polymorph (JCPDS 14-0644) for the fresh sample and from β-MnO_2 polymorph (JCPDS 24-0735) for the sample calcined at 400 °C.

Figure 2 shows the Raman spectra of plasma-precipitated MnO_2 before and after calcination. The two main bands at 571 and 637 cm^{-1}, which are due to stretching and bending vibrations of Mn–O–Mn bonds into 4.6 Å × 4.6 Å tunnels of α-MnO_2 [30, 36], do not show any change after calcination at different temperatures [Fig. 2(a)], which confirms the thermal stability of α-MnO_2 revealed by XRD. Furthermore, the spectrum of γ-MnO_2 after calcination does not show major change [Fig. 2(b)]. Actually, we would have expected a significant change in the spectrum of the material after calcination at 400 °C, provoking a transformation of γ-MnO_2 to β-MnO_2. We recorded indeed a weak shift of the band at 632 (γ-MnO_2) to 630 cm^{-1} (β-MnO_2) [37, 38]. The proximity between both bands

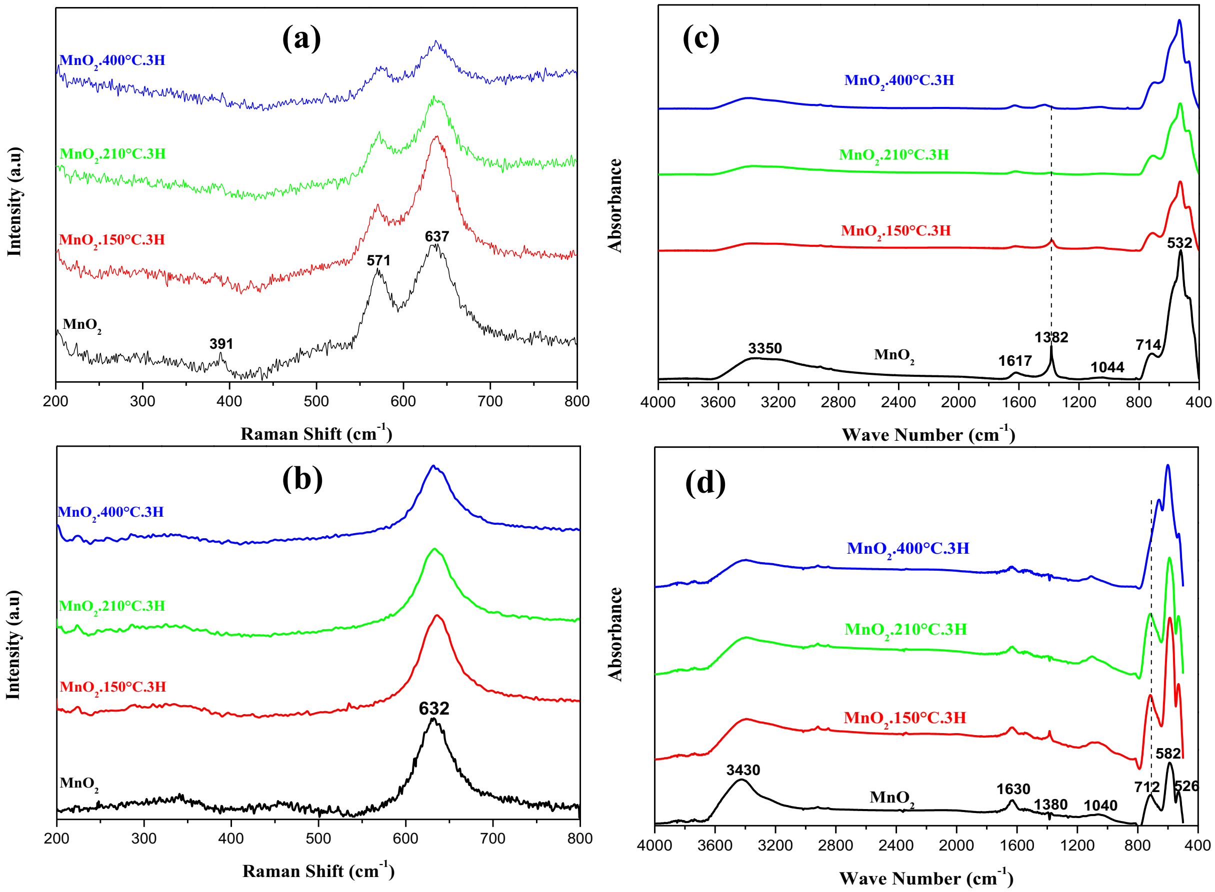

Figure 2: Raman spectra of plasma-precipitated α-MnO_2 (a) and γ-MnO_2 (b) before and after calcination; IR spectra of plasma-precipitated α-MnO_2 (c) and γ-MnO_2 (d) before and after calcination.

could be explained by the fact that the γ-MnO_2 polymorph is the result of the intergrowth of the β-MnO_2 (Pyrolusite) and R-MnO_2 (Ramsdellite) polymorphs [31, 38].

The IR spectra of both plasma-precipitated MnO_2, before and after calcination, are also depicted in Fig. 2. An increase in the calcination temperature of α-MnO_2 revealed, on one hand, a significant decrease of the H–O vibration bond at 1383 cm^{-1} [Fig. 2(c)], which could be ascribed to the removal of the chemisorbed or crystallized water [39, 40]. On the other hand, there was no modification in the absorption bands at 714 and 532 cm^{-1}, which characterize the Mn–O vibration bond. Furthermore, the calcination of γ-MnO_2 shows a regularity of the stretching vibration of the Mn–O bond at 582 cm^{-1} [Fig. 2(d)]. Nevertheless, an absorbance diminution and a shift of the bending vibration of the Mn–O bond at 712 cm^{-1} is recorded after calcination at 400 °C [Fig. 2(d)], which gives an additional evidence of the transformation of γ-MnO_2 to β-MnO_2 [Fig. 1(b)].

A thermogravimetric analysis of fresh and calcined plasma-precipitated α-MnO_2 and γ-MnO_2 has been achieved (Fig. S_1). Both types of MnO_2 show three main mass losses. The first one takes place between 25 and 200 °C, which characterizes the removal of physisorbed water. The second one between 200 and 500 °C is ascribed to the removal of structural or crystallized water [41], which is more present within α-MnO_2 than γ-MnO_2 (Table S_1). The third loss takes place between 500 and 600 °C, which characterizes the phase decomposition of MnO_2 to Mn_2O_3 [42].

The evolution of Mn average oxidation state (AOS) during calcination of both plasma-precipitated MnO_2 has been followed by XPS analysis (Table 1). The gap energy values between $Mn2p_{1/2}$ and $Mn2p_{3/2}$ peaks of the different materials are in accordance with the literature data about MnO_2 [43–45]. The calcination temperature does not significantly affect the AOS of Mn within α-MnO_2, due to the presence of the K element inside its 2 × 2 tunnels [46]. In contrast, the calcination of γ-MnO_2 at 400 °C revealed an augmentation of the AOS of Mn, which corroborates the formation of β-MnO_2, already previously understood. This polymorph is known to have a single and high valence Mn(IV) compared to other polymorphs that have mixed Mn(III, IV) valence [47, 48]. Table S_1 shows the empirical formula of the different materials obtained after merging the TGA and XPS analyses. We observe a reduction

TABLE 1: XPS data of plasma-precipitated MnO_2 before and after calcination.

Material	AOS (Mn)	%K	%C	%Mn	$\%O_\gamma$	$\%O_\alpha$	$\%O_\beta$	O_α/O_β
α-MnO_2	3.61	1.0	21.8	23.1	4.9	6.8	42.4	0.16
α-MnO_2 150.3H	3.60	1.0	26.5	20.8	5.2	7.3	39.2	0.19
α-MnO_2 210.3H	3.51	0.7	28.7	19.4	3.8	8.8	38.6	0.23
α-MnO_2 400.3H	3.54	1.0	27.1	20.8	4.4	6.8	39.9	0.17
γ-MnO_2	3.53	0	32.0	20.0	5.7	6.6	35.7	0.18
γ-MnO_2 150.3H	3.43	0	25.5	20.6	6.5	11.7	35.7	0.33
γ-MnO_2 210.3H	3.48	0	29.1	19.6	6.1	8.6	36.6	0.23
γ-MnO_2 400.3H = β-MnO_2	3.64	0	28.0	20.0	5.3	7.0	39.7	0.18

of structural or crystallized water within each MnO_2 with the increase of calcination temperature. Heating of both MnO_2 at different temperatures does not significantly affect the chemisorbed oxygen density O_α (O_2^{2-}, O^-, HO^-) in binding energy range 531.3–531.8 eV [44, 49], and lattice oxygen density O_β (O^{2-}) in the binding energy 529.7–530.1 eV, and hence the O_α/O_β (the density of oxygen vacant sites) ratio. Otherwise, rearrangement of octahedra within γ-MnO_2 during its conversion to β-MnO_2 after heating at 400 °C [Fig. 1(b)] does not affect its oxygen (lattice and chemisorbed), contrary to what was expected. The oxygen contribution related to contamination carbon (O_γ) falling in the range 532.4–533.2 eV, was calculated from the corresponding contributions found in the C1s signal [20]. But, we focused our attention on chemisorbed and lattice oxygens.

Textural and morphological analyses

The adsorption–desorption isotherms of both plasma-precipitated MnO_2 before and after calcination are depicted on Fig. 3. In all cases type IV isotherms with a hysteresis loop are observed

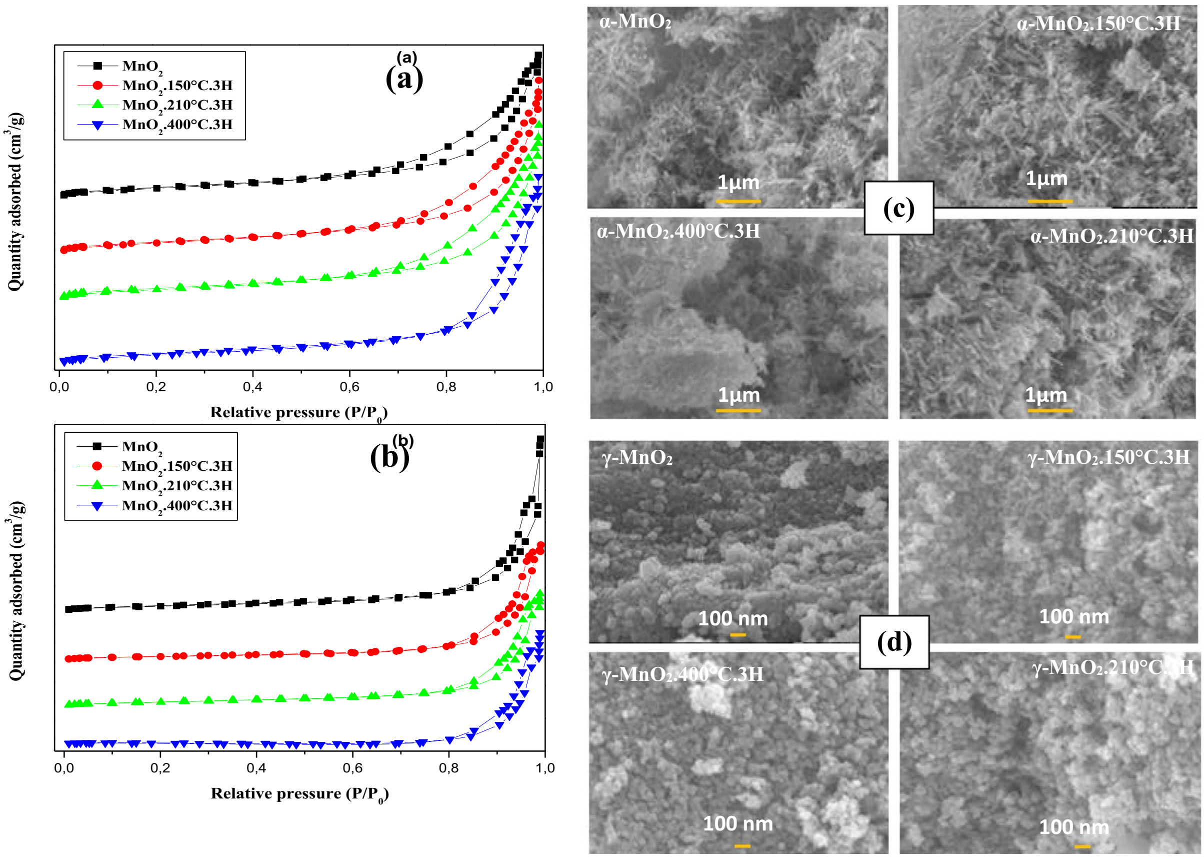

Figure 3: Adsorption–desorption isotherms of both plasma-precipitated α-MnO_2 (a) and γ-MnO_2 (b) before and after calcination; SEM images (× 37,000) of α-MnO_2 (c), γ-MnO_2 (d) before/after treatment calcination.

typical of mesoporous materials [50]. The increase in the calcination temperature of α-MnO_2 revealed a shift of the hysteresis loop towards high relative pressures [Fig. 3(a)], which indicates that capillary decondensation happens within larger pores. The pores diameter distribution of α-MnO_2 (Fig. S_2a) shows an enlargement and a shift of the main peak towards higher diameters when the calcination temperature increases. This could be ascribed to the evolution of α-MnO_2 external mesoporosity towards macroporosity and could reveal an agglomeration of nanorods to larger particles during the calcination. On the other hand, the calcination of γ-MnO_2 revealed that the position of the two maxima at 15 and 35 nm remained unchanged (Fig. S_2b), which corroborates a stable position of the hysteresis loop after calcination at the different temperatures [Fig. 3(b)]. Otherwise, the peak at 15 nm could be ascribed to the external mesoporosity between small nanospheres, while the one at 35 nm to the external mesoporosity between large nanospheres [Fig. 3(d)]. Table 2 summarizes the textural data of the different materials. We recorded a decrease in the specific surface area of both plasma-precipitated MnO_2, which is due to the described evolution of the pores when increasing the calcination temperature [51]. This decrease of the specific surface area is less important for α-MnO_2 than γ-MnO_2, which could be explained thanks to the presence of K^+ within α-MnO_2, protecting the lattice oxygen O_β during the calcination as can be seen in Table 1. This result highlights the fact that the evolution of pore size during calcination of both MnO_2, strongly depends on its morphology (Fig. 3). Therefore, textural properties of γ-MnO_2 are more affected than those of α-MnO_2 after calcination.

Figure 3 also shows SEM images of both fresh plasma-precipitated and calcined MnO_2. Morphology of α-MnO_2 polymorph is not affected after calcination at 150 and 210 °C [Fig. 3(c)]. On the other hand, calcination at 400 °C induces a merging of nanorods to agglomerates with a diameter range of 50–100 nm and length range of 50–300 nm. The significant increase in diameter after heating of α-MnO_2 at 400 °C is in accordance with the increase of pores diameter as revealed by nitrogen physisorption analysis (Table 2). However, no significant change of morphology is recorded after heating of γ-MnO_2 nanospheres [Fig. 3(d)] up to 400 °C. This fact agrees with the non-modified peaks at 15 and 35 nm in the pore diameter distribution of this series of samples (Fig. S_2b).

TABLE 2: Textural data of different materials.

Material	Specific surface area (m^2/g)	Pores diameter (nm)	Pores volume (cm^3/g)
α-MnO_2	98	12	0.33
α-MnO_2.150.3H	90	14	0.34
α-MnO_2.210.3H	88	14	0.34
α-MnO_2.400.3H	85	17	0.41
γ-MnO_2	48	29	0.34
γ-MnO_2.150.3H	38	23	0.24
γ-MnO_2.210.3H	35	21	0.22
γ-MnO_2.400.3H = β-MnO_2	22	25	0.22

Catalytic tests

To assess the impact of the initial pH of the solution on the catalytic bleaching process of TY, knowing its importance during the adsorption step of the pollutant, catalytic treatment of TY has been performed at different initial pH with plasma-synthesized α-MnO_2 not-calcined as catalyst. Results depicted on figure S_3, show an increase of the bleaching efficiency of TY with decrease of the initial pH of the solution. This efficiency could be attributed to the acid–base properties in solution of plasma-precipitated α-MnO_2. At pH > ZPC (Zero-point charge of MnO_2 ~ 4.4) [20], the catalyst is negatively charged, and electrostatic repulsion is assumed between the catalyst and the sulfonate functions of the pollutant (negatively charged, Fig. S_4), resulting in inefficiency of the catalytic process. At contrary, at pH < ZPC, an electrostatic attraction is assumed between the negative charges of the pollutant and the positive charges of the catalyst, thus a strong adsorption between the two entities, and consequently a significant catalytic bleaching of TY. If we consider the range time between 0 and 45 min as the adsorption phase (first step of the catalytic process), we could observe at pH 2.5, a highest adsorption degree (83%) compared to those obtained at pH values of 3.0 (21%), 3.5 (9%) and 5.0 (0%). Based on this, pH 2.5 is the best and will be used for the rest of study. Following the evolution of the catalytic bleaching degree with reaction time (Fig. S_3), a complete bleaching of TY (100%) is reached after 180 min, even if we can observe a leveling of the curve (low variation) from 100 min. Hence, the following catalytic tests have been performed at pH 2.5 and 180 min as reaction time.

However, the degradation of TY after adsorption phase has already been elucidated in our previous publication [19], where we analysed the catalyst after TY treatment via FTIR analysis, knowing that in the case of an adsorption process only, the pollutants absorption band should appear on the IR spectrum of the catalyst after treatment, which was not the case [20]. Moreover, to deeply show that the removal of TY in solution is not limited to the adsorption process, we carried out some analysis, such as UV–vis, Chemical demand oxygen (COD), High performance liquid chromatography (HPLC), on the withdrawn solution after catalytic bleaching of TY, which reinforced the previous discussion, even if we did not have possibility to identity generated by-products [20]. As we can see through Table 1, all plasma-precipitated MnO_2 (calcined or not) have Mn in mixed valence Mn (III, IV), following their respective average oxidation state (AOS) values. This generates structural defects or oxygen vacant sites (activation sites) able to interact with water via dissociation producing HO· species. On the other hand, electrons produced during the collision of particles under magnetic stirring, will react with dissolved oxygen to generate HO_2 species [20]. Both radicals, are susceptible to mineralize TY molecule in solution through mechanism depicted on Figure S_5. [19] elucidate the production of HO· species using hydroxyls scavengers such as KI and n-butanol [20].

Figure 4 shows the impact of the calcination temperature on the catalytic activity of the plasma-precipitated MnO_2. A slight decrease in the bleaching efficiency of TY on α-MnO_2 occurs when its calcination temperature rises [Fig. 4(a)], in agreement with the diminution of its specific surface area after calcination (Table 2). The linear relationship between them suggests that the loss of activity is only due to the loss of specific surface area and not to any structural event. This could be ascribed to the consolidation of the α-MnO_2 crystalline structure by the presence of K within the large 4.6 Å × 4.6 Å tunnels. At the opposite an increase in calcination temperature of γ-MnO_2 provokes two significant decreases of the TY bleaching efficiency [Fig. 4(b)]. The first one occurs after heating of γ-MnO_2 at 150 °C which is in accordance with the drop of its specific surface area after calcination (Table 2). The second one occurs after heating of γ-MnO_2 at 400 °C which could be ascribed to two facts: in addition to the drop of the specific surface area, the smaller tunnels 2.3 Å × 2.3 Å of β-MnO_2 polymorph (γ-MnO_2.400 °C.3H, material obtained after heating of γ-MnO_2 at 400 °C) reduce the possibility of catalytic oxidation of TY to occur within its tunnels, explaining the significant decrease of the catalytic bleaching. These results show the relationship between the crystalline and activity stabilities of plasma-precipitated MnO_2.

Stability of plasma-precipitated MnO_2 after catalytic bleaching of Tartrazine yellow

Characterization of fresh and used catalysts

The stability of the two polymorphs during catalytic treatment was also studied. Figure 5a shows XRD patterns of plasma-precipitated α-MnO_2 and γ-MnO_2 before and after use. The α-MnO_2 patterns before and after bleaching of TY show the same diffraction peaks. For γ-MnO_2, the diffraction peaks slightly decrease in intensity, and diffraction peaks at 34.9° (031) and 62.6° (401) totally disappeared after the bleaching of TY. The α-MnO_2 polymorph reveals higher crystalline stability than γ-MnO_2 polymorph during the bleaching of TY. This again could be ascribed to the presence of the K^+ ions within 4.6 Å × 4.6 Å tunnels of α-MnO_2 as compared to γ-MnO_2 for which those ions are absent. Moreover, the leaching test of both catalysts during the bleaching of TY has been explored (Fig. S_6). Both materials underwent a weak release of Mn in the medium likely because of its strong acidity (pH 2.5) which was favourable to the acid attack of the oxide. Nevertheless, the α-MnO_2 polymorph was less leached than γ-MnO_2, in line with its higher crystalline stability as previously understood by XRD [Fig. 5(a)]. It is also worthy to point that the release of Mn took place only during the five first minutes of the test, and then stabilization is observed.

The IR spectra of the pollutant TY, those of each catalyst, before and after bleaching, are depicted in figure S_7. There is no pollutant absorption band on the spectra of any catalysts after bleaching test. This allows discarding the hypothesis of the disappearance of TY along the test could be due to its simple adsorption on both catalysts surfaces. In contrast, a disappearance of the absorption band at 1382 cm^{-1} on the α-MnO_2 spectrum after treatment (Fig. S_6a) could illustrate

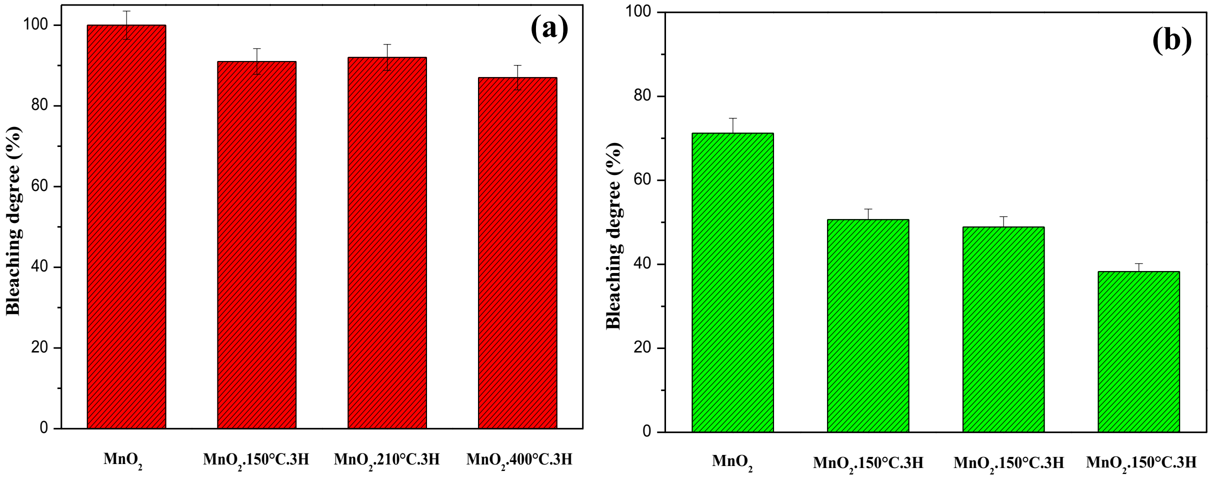

Figure 4: Bleaching evolution of TY (T* = 180 min, pH 2.5) with plasma-precipitated α-MnO_2 (a) and γ-MnO_2 (b) before and after calcination.

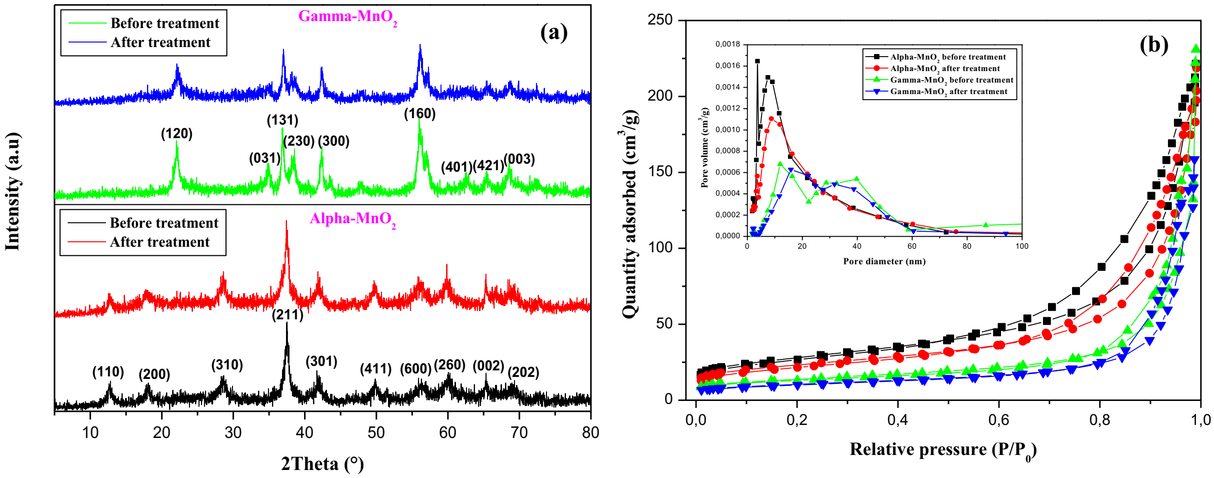

Figure 5: (a) XRD patterns, (b) Adsorption–desorption isotherms and pores size distribution of fresh and used plasma-precipitated α-MnO_2 and γ-MnO_2.

the removal of (chemisorbed or crystallized) water within the 4.6 Å × 4.6 Å and 2.3 Å × 2.3 Å tunnels that exists in that polymorph [52], and which would be induced by the adsorption of the pollutant at its place.

Figure S_8 depicts XPS surveys spectra of plasma-precipitated MnO_2 before and after the catalytic bleaching of TY. There is a decrease in peak intensity of K (Fig. S_8a,b), which could be due to the gradual removal of K within the 4.6 Å × 4.6 Å tunnels of α-MnO_2 [53] after treatment. FTIR and XPS surveys spectra of both catalysts after catalytic bleaching of TY did not reveal any presence of pollutant, and deeply confirm the degradation of TY after adsorption phase. Table S_2 summarizes the XPS data of the different materials. A diminution of the Mn average oxidation state (AOS) in each catalyst is observed. This could be ascribed to the presence of small amount of Mn^{2+} or an increase of the Mn^{3+} amount in each catalyst after the slight leaching of both materials [54]. There is also a slight decrease in lattice oxygen density O_β within α-MnO_2 after catalytic bleaching of TY, which could illustrate the participation of some oxygens during the catalytic process. On the other hand, an increase of chemisorbed oxygen density O_α is recorded in both catalysts, which could be due to the oxygen fixation from the aqueous medium. Figure 5b represents the adsorption–desorption isotherms and pores diameter distribution of the tested materials, which show a hysteresis loop and type IV, characteristic of mesoporous solids [52]. A slight shift of the hysteresis loop towards high relative pressures is also observed, which means an augmentation of the pores size after bleaching of TY with each MnO_2. Table 3 shows the textural data of both catalysts, before and after bleaching test of TY, which reveals a drop of their specific surface area. Figure S_7 shows the SEM images of both catalysts before and after treatment of TY. No change of morphology is recorded after the bleaching of TY with α-MnO_2 nanorods (Fig. S_9a,b) and γ-MnO_2 nanospheres (Fig. S_9c,d).

TABLE 3: Textural data of different materials before and after catalytic test.

Catalyst	Specific surface area (m^2/g)	Pores diameter (nm)	Pores volume (cm^3/g)
α-MnO_2 Before	98	12	0.33
α-MnO_2 After	80	15	0.31
γ-MnO_2 Before	48	29	0.33
γ-MnO_2 After	36	23	0.23

Reuse of both catalysts after the first catalytic test

In our previous studies [20], we reported a quasi-constant catalytic activity of the α-MnO_2 polymorph obtained via gliding arc plasma-reduction of $KMnO_4$, due to the consolidation of its crystalline structure thanks to the presence of K within its 4.6 Å × 4.6 Å tunnels, and this despite a decrease of its specific surface area after the first cycle [20]. This behavior is confirmed in the present study (Table 3). However, we did not compare yet this behavior with a MnO_2 polymorph without any cationic species within its crystalline structure. Therefore, Fig. 6 depicts the respective evolution of the catalytic bleaching of TY after 4 cycles ($T^* = 180$ min) with plasma-precipitated α-MnO_2 [Fig. 6(a)] [20] and with γ-MnO_2 which does not contain any cationic species [Fig. 6(b)], as catalysts. In contrast to α-MnO_2, γ-MnO_2 revealed a diminution of the catalytic bleaching of TY after the first cycle, which corroborates a decrease in its specific surface area (Table 3). However, the amorphicity of γ-MnO_2 after treatment [Fig. 5(a)] could also explain its activity loss after the first cycle. Uematsu et al. showed that α-MnO_2 can efficiently

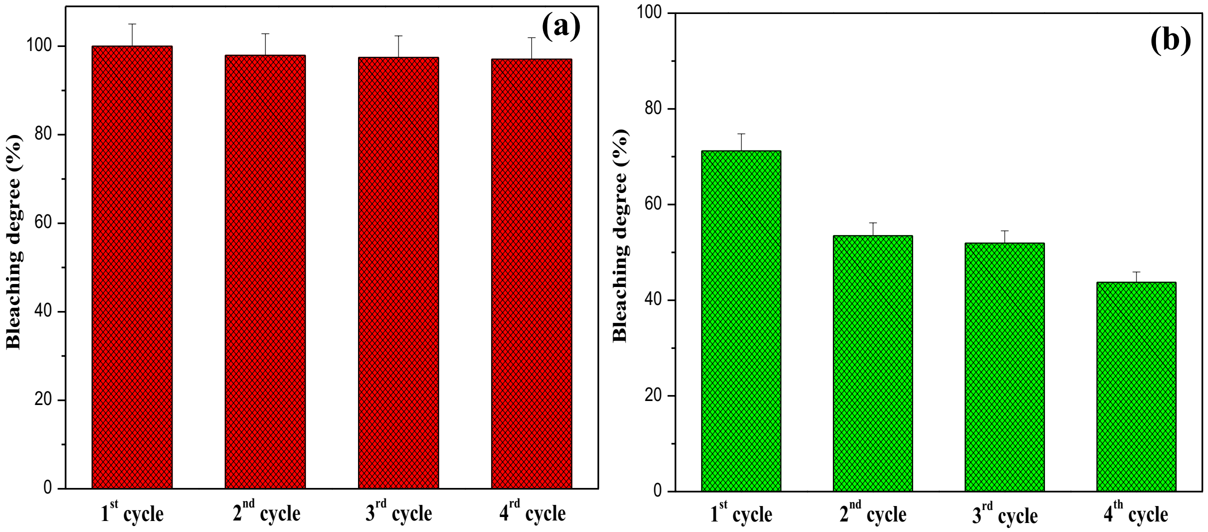

Figure 6: Use of plasma-precipitated α-MnO_2 (a) and γ-MnO_2 (b) for 4 catalytic cycles (T* = 180 min, pH 2.5).

be reused as catalyst for the aerobic oxygenation of sulfur to sulfoxides during 4 cycles. Indeed, this polymorph has a greater catalytic stability, compared to γ-MnO_2, β-MnO_2, and δ-MnO_2 polymorphs [55]. Additionally, Liu et al. reported that α-MnO_2 prepared via the hydrothermal route, can be reused for 3 cycles during the Rhodamine B degradation [56]. In contrast, Fathy et al. established that γ-MnO_2/MWCNT nanocomposites, used as catalysts for the Reactive Blue 19 oxidation, have their activity decreased after the first cycle, and this diminution is more pronounced after 4 cycles [57]. This means that the insertion of cationic species into MnO_2 crystalline structure during its synthesis via plasma glidarc route could allow a high stability of its structure and activity.

To gain deeper insights into this, we have by purpose inserted some cations within MnO_2 structure during its synthesis. This consisted in precipitating $KMnO_4$, $NaMnO_4$ and $Mg(MnO_4)_2$ solutions (700 mg/L) via their reduction along the gliding arc plasma route. Afterwards, the three obtained materials were used as catalyst during four catalytic bleaching cycles of TY. Table S_3 shows the three plasma-precipitated MnO_2, with the inserted cationic species (Na^+, Mg^{2+} and K^+). A quasi-stable activity of the three modified MnO_2 as catalysts during four catalytic cycles was observed (Fig. 7). This result further highlights the positive impact of the cationic insertion within plasma-precipitated MnO_2 on its activity. The efficiency of catalytic bleaching process of TY, due to cationic species doping material, could be explained following two aspects. (i) Firstly, insertion of cationic species within the tunnel of MnO_2 generates oxygen vacant sites (activation sites), which will interact with water and dissolved oxygen (without adding of H_2O_2), producing powerful oxidizing species such as HO· and HO_2· radicals. (ii) Secondly, the cationic doping, allows the stabilization of the crystalline structure of the catalyst during calcination and many reuse tests (catalytic cycles).

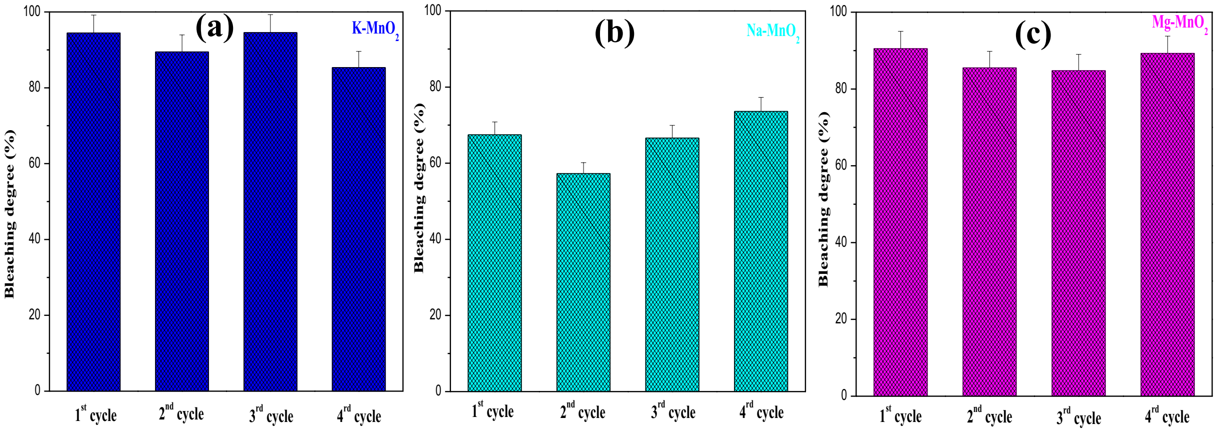

Figure 7: Catalytic bleaching of TY (T* = 180 min, pH 2.5) with modified (a) K-MnO_2, (b) Na-MnO_2 and (c) Mg-MnO_2.

Conclusion

The plasma-precipitated α-MnO_2 nanorods showed a higher crystalline stability than the γ-MnO_2 nanospheres after calcination at high temperature. We recorded a greater catalytic stability of α-MnO_2 than γ-MnO_2, despite their both decrease of specific surface areas after calcination at different temperatures. Otherwise, plasma-precipitated α-MnO_2 shows a greater crystalline and catalytic stability than γ-MnO_2, during the catalytic bleaching of Tartrazine Yellow (TY). Modification of MnO_2 structure through the insertion of cationic species during its synthesis by gliding arc plasma leads to the stability of its structure and activity. Therefore, this work highlights the relationship between crystalline structure and catalytic stabilities of plasma-precipitated MnO_2. Gliding arc plasma appears as an innovative route allowing the stabilization of MnO_2 structure and activity via some cationic species during its synthesis without adding any reactant as is the case with the classical methods.

Material and methods

Synthesis procedure

$KMnO_4$ (97% wt), $Mn(CH_3COO)_3.2H_2O$ (97% wt), $Mg(MnO_4)_2$ and $NaMnO_4$ (40% wt in H_2O) were purchased from SIGMA-ALDRICH. Preparation of the precursors solutions consisted to dissolving 1.4 g of $KMnO_4$ in 2L of de-ionized water, and 1 g of $Mn(CH_3COO)_3.2H_2O$ in 500 mL of a mixture of acetic acid (95% wt) and de-ionized water (ratio 1/21). The target solutions of $KMnO_4$ (450 mL, 700 mg/L), and $Mn(CH_3COO)_3.2H_2O$ (450 mL, 2000 mg/L) were then exposed to the plasma discharge (Fig. S_{10}) previously described [16], during 28 and 15 min, respectively, both at ambient conditions and under magnetic stirring. Brown-black precipitates were obtained after the respective exposures and recovered by simple filtration. Then, they were washed with de-ionized water, and dried at 105 °C under air. The plasma-precipitated materials were heated under air in an oven for 3 h at 150 °C, 210 °C and 400 °C.

Characterization techniques

X-ray diffraction patterns of the different materials were recorded between 5 and 80° at the rate of 0.5°/ min with an increment of 0.02° and an integration time of 2 s using a Kristallofex SIEMENS D5000 diffractometer, operating at 40 kV and 40 mA, with Cu K_α radiation (1.5418 Å). The powdered samples were deposited on zero noise polished Si sample holders previously cleaned and slightly impregnated with handcream. The ICDD-JCPDS database was used to identify the crystalline phases. Raman spectroscopy analysis was carried out on 2 mg of sample using a Bruker RFS 100IS, equipped with a 532 nm excitation laser (10 mW), and working with 4 cm^{-1} as resolution. Raman spectra were collected after 5 scans using a confocal spectrometer, with a magnification objective of 10x, a spot size of 100 microns; acquisition time was 15 s. Fourier transform infrared spectroscopy was recorded in transmission mode after 100 scans, at a resolution of 4 cm^{-1}, employing an Equinox IFS55 spectrometer (Bruker), equipped with a DTGS detector. The pellets were made by diluting the samples in KBr (2 mg of sample for 200 mg of KBr), and then pressing them into self-supporting disks using a hydraulic press (5–7.5 bar) for about 5 min. Atmospheric air spectrum has been used as a reference. Thermogravimetric analysis was performed on a thermo-analyzer Mettler Toledo TGA/SDTA 851 TA Instruments SDT 2960, under air (100 mL/min) in the temperature range from 25 to 900 °C, at a heating rate of 10 °C/min. X-ray photoelectron spectroscopy was carried out using SSX 100/206 photoelectron spectrometer from Surface Science Instruments (USA) equipped with a 30° solid acceptance lens, a hemispherical analyser, and a monochromatic source of Al K_α (1486.6 eV) operated at 15 kV and 10 mA, at a pressure of about 10^{-6} Pa within the analysis chamber. The angle between the surface normal and the axis of the analyser lens was 55°. The analysed area was approximately 1.4 mm^2 and the pass energy was set at 150 eV. In these conditions, the full width at half maximum (FWHM) of the Au $4f_{7/2}$ peak of a clean gold standard sample was about 1.6 eV. A flood gun set at 8 eV and a nickel (Ni) grid placed 3 mm above the sample surface were used for charge stabilisation. The sample powder was pressed in small stainless-steel troughs of 4 mm diameter and placed on an aluminium conductive carousel. Before analysis, all samples were outgassed under vacuum (10^{-5} Pa) for 24 h to remove the physisorbed compounds. The binding energy range was calibrated taking the carbon C1s peak fixed at 284.8 eV (aliphatic component of carbon contamination), as reference. The atomic ratios were obtained using a normalized peak area based on the acquisition parameters and experimental sensitivity factors provided by the manufacturer. The Mn2p region was used to quantify Mn proportion. While those of lattice oxygen (structural) and chemisorbed oxygen (surface) were decomposing the O1s signal after deducing the oxygen-related to carbon contamination. The average oxidation state (AOS) of Mn was determined using the shift of the Mn3s binding energy [58, 59], following Eq. 1, where ΔE_s represents the shift of the binding energy between Mn3s and its satellite [60].

$$AOS = 8.956 - 1.126\Delta E_s \quad (1)$$

Nitrogen physisorption was carried out at -196 °C using a Micromeritics Tristar 3000 in the relative pressure range [10^{-6}-0.99]. Before analysis, 150 mg of sample was outgassed at 150 °C for 12 h, under primary vacuum. The specific surface area and pore size distribution were calculated using Brunauer–Emmett–Teller (BET) equation in the 0.05–0.30 P/

P_0 range and the Barrett-Joyner-Halenda (BJH) method, respectively. Error on the specific surface area was determined by calculating the standard deviation on a series of values related to 3 analyses of the same sample. The morphology was investigated using a LEO 983 GEMINI scanning electron microscope operated at an acceleration voltage between 10 and 15 kV, depending on the sample. Before analysis, the samples were metalized under an argon atmosphere with a layer about 15 nm thick of chromium.

Catalytic test, recovery, and reuse of catalyst

All the tests were carried out using Tartrazine Yellow (TY) as a representative azoic organic dye (Fig. S_4), which is employed in many industries such as food, medicine, and cosmetics manufacturing, and often found in their wastewaters [61].

Standard catalytic tests were performed in a batch reactor in the absence of light by wrapping the reactor using aluminium foil, and at room temperature (~ 25 °C), with dissolved oxygen as oxidizing agent [20]. The tests consisted in introducing 100 mL of TY solution (20 mg/L) into the reactor, then adjusting the pH solution to 2.5 using H_2SO_4 (0.1 M) and adding 50 mg of catalyst under magnetic stirring. About 2 mL of the reaction medium was withdrawn using a syringe, at defined time intervals, and then filtrated. The residual concentration of TY was analysed at 425 nm with a GENESYS 10S spectrophotometer, through a calibration absorbance-concentration curve. The bleaching degree (%D) was calculated using Eq. 2, where C_0 and C_t, respectively, represent initial and residual concentrations of TY at defined times. All these tests were carried out in a dark environment.

$$\%D = [(C_0 - C_t)/C_0] \times 100 \tag{2}$$

All the catalysts recovered after each test were characterized by XRD, FTIR, XPS, nitrogen physisorption analysis, and SEM, as described above. The reusability of the samples was carried out for 4 catalytic cycles.

Acknowledgments

We are grateful to the “Université catholique de Louvain” for scholarship given to F.W. Boyom Tatchemo from the “Coopération au développement” program.

Author contributions

FWBT: Investigation, Conceptualization, Methodology, Data treatment and interpretation, Writing—original draft, Writing—review & editing. FD: XPS characterization, Data treatment and review. EA: Review & editing. GKY: Review & editing. SN: Review & editing. SL: Resources, Supervision. EG: Funding acquisition, Project administration, Conceptualization, Supervision, Data treatment and interpretation, Resources, Writing—review & editing, Validation.

Funding

Université Catholique de Louvain.

Data availability

All data generated or analyzed during this study are included in this published article (and its supplementary information files).

Declarations

Conflict of interest On behalf of all authors, the corresponding author states that there is no conflict of interest.

Supplementary Information

The online version contains supplementary material available at https://doi.org/10.1557/s43578-023-01129-z.

References

1. X.F. Guo, G.J. Kim, Synthesis of ordered mesoporous manganese oxides by double replication for use as an electrode material. Bull. Korean Chem. Soc. **32**, 186–190 (2011). https://doi.org/10.5012/bkcs.2011.32.1.186
2. C. Wang, R. Yan, M. Cai, Y. Liu, S. Li, Appl. Surf. Sci. **610**, 155346 (2023). https://doi.org/10.1016/j.apsusc.2022.155346
3. M. Cai, Y. Liu, C. Wang, W. Lin, S. Li, Novel $Cd_{0.5}Zn_{0.5}S$/$Bi2MoO_6$ S-scheme heterojunction for boosting the photodegradation of antibiotic enrofloxacin: Degradation pathway mechanism and toxicity assessment. Sep. Purif. Technol. **304**, 122401 (2023). https://doi.org/10.1016/j.seppur.2022.122401
4. M. Cai, C. Wang, Y. Liu, R. Yan, S. Li, Boosted photocatalytic antibiotic degradation performance of $Cd_{0.5}Zn_{0.5}S$/carbon dots/$Bi2WO_6$ S-scheme heterojunction with carbon dots as the electron bridge. Sep. Purif. Technol. **300**, 121892 (2022). https://doi.org/10.1016/j.seppur.2022.121892
5. S. Li, M. Cai, Y. Liu, C. Wang, R. Yan, X. Chen, Constructing $Cd_{0.5}Zn_{0.5}S$/$Bi2WO_6$ S-scheme heterojunction for boosted photocatalytic antibiotic oxidation and Cr(VI) reduction. Adv. Powder. Mater. **2**, 100073 (2023). https://doi.org/10.1016/j.apmate.2022.100073
6. S. Li, M. Cai, C. Wang, Ta_3N_5/CdS Core-Shell S-scheme Heterojunction Nanofibers for Efficient Photocatalytic Removal of Antibiotic Tetracycline and Cr(VI): Performance and Mechanism Insights. Adv. Fiber Mater. **5**, 994–1007 (2023). https://doi.org/10.1007/s42765-022-00253-5
7. C. Hongmin, P.K. Chu, J.H. He, T. Hu, M. Yang, Porous magnetic manganese oxide nanostructures: synthesis and their

applications in water treatment. J. Colloid Interface Sci. **359**, 68–74 (2011). https://doi.org/10.1016/j.jcis.2011.03.089

8. H.J. Wang, X.Y. Chen, Kinetic analysis and energy efficiency of phenol degradation in a plasma-photocatalysis system. J. Hazard. Mater. **186**, 1888–1892 (2011). https://doi.org/10.1016/j.jhazmat.2010.12.088
9. S. Li, C. Wang, Y. Liu, Y. Liu, M. Cai, W. Zhao, X. Duan, Chem. Eng. J. **455**, 140943 (2023). https://doi.org/10.1016/j.cej.2022.140943
10. J. Dai, S.F.Y. Li, K.S. Siow, Z. Gao, Synthesis and characterization of the hollandite-type MnO_2 as a cathode material in lithium batteries. Electrochim. Acta **45**, 2211–2217 (2000). https://doi.org/10.1016/S0013-4686(99)00441-7
11. J. Zhao, Z. Tao, J. Liang, J. Chen, Facile synthesis of γ-MnO_2 structures and their applications in rechargeable Li-ion batteries. Cryst. Growth Des. **8**(8), 2799–2805 (2008). https://doi.org/10.1021/CG701044B
12. J. Liu, Y. Son, J. Cai, X. Shen, S. Suib, M. Aindow, Size control, metal substitution, and catalytic application of cryptomelane nanomaterials prepared using cross-linking reagents. Chem. Mater. **16**, 276–285 (2004). https://doi.org/10.1021/cm0303989
13. V. Subramanian, H. Zhu, B. Wie, Alcohol-assisted room temperature synthesis of different nanostructured manganese oxides and their pseudocapacitance properties in neutral electrolyte. Chem. Phys. Lett. **453**, 242–249 (2008). https://doi.org/10.1016/j.cplett.2008.01.042
14. S.H. Kim, S.J. Kim, M.O. Seung, Preparation of layered MnO_2 via thermal decomposition of $KMnO_4$ and its electrochemical characterizations. Chem. Mater. **11**, 557–563 (1999). https://doi.org/10.1021/CM9801643
15. K.A.M. Ahmed, H. Peng, K. Wu, K. Huang, Hydrothermal preparation of nanostructured manganese oxides (MnO_x) and their electrochemical and photocatalytic properties. Chem. Eng. J. **172**, 531–539 (2011). https://doi.org/10.1016/j.cej.2011.05.070
16. X. Zhang, P. Yu, H. Zhang, D. Zhang, X. Sun, Y. Ma, Rapid hydrothermal synthesis of hierarchical nanostructures assembled from ultrathin birnessite-type MnO_2 nanosheets for supercapacitor applications. Electrochim. Acta **89**, 523–529 (2013). https://doi.org/10.1016/j.electacta.2012.11.089
17. Y. Li, J. Wang, Y. Zhang, M. Banis, J. Liu, D. Geng, R. Li, X. Sun, Facile controlled synthesis and growth mechanisms of flower-like and tubular MnO_2 nanostructures by microwave-assisted hydrothermal method. J. Colloid Interface Sci. **369**, 123–128 (2012). https://doi.org/10.1016/j.jcis.2011.12.013
18. E. Acayanka, D.S. Kuete, G.Y. Kamgang, S. Nzali, S. Laminsi, P.T. Ndifon, Synthesis, characterization and photocatalytic applications of TiO_2/SnO_2 nanocomposite obtained under non-thermal plasma condition at atmospheric pressure. Plasma Chem. Plasma Process. **36**, 799–811 (2016). https://doi.org/10.1007/s11090-016-9699-0
19. F.W. Boyom-Tatchemo, S. Nzali, G. Kamgang-Youbi, A. Tiya-Djowe, D. Kuete-Saa, E. Acayanka, S. Laminsi, E.M. Gaigneaux, Gliding arc plasma synthesis of MnO_2 nanorods for the plasma-catalytic bleaching of azoic Amaranth Red dye. Top. Catal. **60**, 962–972 (2017). https://doi.org/10.1007/s11244-017-0761-9
20. F.W. Boyom-Tatchemo, F. Devred, G. Ndiffo-Yemeli, S. Laminsi, E.M. Gaigneaux, Plasma-induced reactions synthesis of nano-sized α-, γ- and δ-MnO_2 catalysts for dye degradation. Appl. Catal. B: Environ. **26**, 118159 (2020). https://doi.org/10.1016/j.apcatb.2019.118159
21. R. Kannan, K. Govindan, S. Selvaraj, P. Ravichandiran, S. Vasanthkumar, Birnessite nanorod-mediated decomposition of methylene blue with common oxidants. Appl. Water. Sci. **3**, 335–341 (2013). https://doi.org/10.1007/s13201-012-0058-x
22. A.H. Germeay, R.G. El-Sharkawy, I.A. Mansour, A.B. Zaki, Catalytic activity of polyaniline/MnO_2 composites towards the oxidative decolourization of organic dyes. Appl. Catal. B: Environ. **80**, 106–115 (2008). https://doi.org/10.1016/j.apcatb.2007.11.014
23. S. Hamoudi, A. Sayari, K. Belkacemi, L. Bonneviot, F. Larachi, Catalytic wet oxidation of phenol over $Pt_xAg_{1-x}MnO_2$/CeO_2 catalysts. Catal. Today **62**, 379–388 (2000). https://doi.org/10.1016/S0920-5861(00)00439-9
24. S.-L. Chiam, S.-Y. Pung, F.-Y. Yeoh, Recent developments in MnO_2-based photocatalysts for organic dye removal: a review. Environ. Sci. Pollut. Res **27**, 5759–5778 (2020). https://doi.org/10.1007/s11356-019-07568-8
25. W. Gong, X. Meng, X. Tang, P. Ji, Core-shell MnO_2-SiO_2 nanorods for catalyzing the removal of dyes from water. Catalysts **7**, 19 (2017). https://doi.org/10.3390/catal7010019
26. A.M. Hashem, H.M. Abuzeid, D. Mikhailova, H. Ehrenberg, A. Mauger, C.M. Julien, Structural and electrochemical properties of α-MnO_2 doped with cobalt. J. Mater. Sci. -Mater. Electron. **47**, 2479–2485 (2012). https://doi.org/10.1007/s10853-011-6071-x
27. F. Teng, S. Santhanagopalan, D.D. Meng, Microstructure control of MnO_2/CNT hybrids under in-situ hydrothermal conditions. Solid State Sci. **12**, 1677–1682 (2010). https://doi.org/10.1016/j.solidstatesciences.2010.07.026
28. J. Wu, H. Huang, L. Yu, J. Hu, Controllable hydrothermal synthesis of MnO_2 nanostructures. Adv. Mater. Phys. Chem. **3**, 201–205 (2013). https://doi.org/10.4236/ampc.2013.33029
29. D. Portehault, S. Cassaignon, E. Baudrin, J.-P. Jolivet, Morphology control of cryptomelane type MnO2 nanowires by soft chemistry. Growth mechanisms on aqueous medium. Chem. Mater. **19**(22), 5410–5417 (2007). https://doi.org/10.1021/cm071654a
30. A.K. Sinha, M. Pradhan, T. Pal, Morphology evolution of two-dimensional MnO_2 nanosheets and their shape transformation to one-dimensional ultralong MnO_2 nanowires for robust catalytic activity. J. Phys. Chem. C **117**, 23976–23986 (2013). https://doi.org/10.1021/jp403527p

31. F.W. Boyom-Tatchemo, F. Devred, S. Laminsi, E.M. Gaigneaux, Temporal post-discharge reactions effect on the oxidative catalytic properties of plasma-precipitated α-MnO_2 nanorods. Appl. Catal., A **616**, 118109 (2021). https://doi.org/10.1016/j.apcata.2021.118109
32. D. Zheng, S. Sun, W. Fan, H. Yu, C. Fan, G. Cao, Z. Yin, X. Song, One-step preparation of single-crystalline β-MnO_2 nanotubes. J. Phys. Chem. B **109**, 16439–16443 (2005). https://doi.org/10.1021/jp052370l
33. C. Ze-hua, H. Ke-Long, L. Su-Qin, W. Hai-Yan, Preparation and characterization of spinel $LiMn_2O_4$ nanorods as lithium-ion battery cathodes. Trans. Nonferrous Met. Soc. China **20**, 2309–2313 (2010). https://doi.org/10.1016/S1003-6326(10)60646-2
34. A.K. Thapa, Y. Hidaka, H. Hagiwara, S. Ida, T. Ishihara, Mesoporous β-MnO_2 air electrode modified with Pd for rechargeability in lithium-Air battery. J. Electrochem. Soc. **158**(12), A1483–A1489 (2011). https://doi.org/10.1149/2.090112jes
35. M.W. Dose, S.W. Donne, Kinetic analysis of γ-MnO_2 thermal treatment. J. Therm. Anal. Calorim. **105**, 113–122 (2011). https://doi.org/10.1007/s10973-011-1445-5
36. J. Luo, H.T. Zhu, H.M. Fan, J.K. Kang, H.L. Shin, G.H. Rao, J.B. Li, Z.M. Du, Z.X. Shen, Synthesis of single-crystal tetragonal α-MnO_2 nanotubes. J. Phys. Chem. Lett. **112**, 12594–12598 (2008). https://doi.org/10.1021/jp8052967
37. X. Huang, C. Pan, X. Huang, Preparation and characterization of γ-MnO_2/CNTs nanocomposite. Mater. Lett. **61**, 934–936 (2007). https://doi.org/10.1016/j.matlet.2006.06.040
38. Y. Xiong, Y. Xie, Z. Li, C. Wu, Growth of well-aligned γ-MnO_2 monocrystalline nanowires through a coordination-polymer-precursor route. Chem. Eur. J. **9**(7), 1645–1651 (2008). https://doi.org/10.1002/chem.200390189
39. S. Saha, A. Pal, Microporous assembly of MnO_2 nanosheets for malachite green degradation. Sep. Sci. Technol. **134**, 26–36 (2014). https://doi.org/10.1016/j.seppur.2014.07.021
40. P. Zhang, X. Li, Q. Zhao, S. Liu, Synthesis and optical property of one-dimensional spinel $ZnMn_2O_4$ nanorods. Nanoscale Res. Lett. **6**(1), 323 (2011). https://doi.org/10.1186/1556-276X-6-323
41. M.A. Ahmed-Hashem, Preparation, characterization, and electrochemical performance of γ-MnO_2 and $LiMn_2O_4$ as cathodes of lithium batteries. Ionics **10**, 206–212 (2004). https://doi.org/10.1007/BF02382818
42. - D. Dias, R. Monteiro, C. Mota-Caetano, A. Pimentel, E. Fortunato, Study of MnO_2 coverage on Ta capacitors with high CV powders, Electronics Components, Assemblies, and Materials Association, Symposium, October-November 2007, Barcelona, Spain (2007), Doi: Rui Monteiro.
43. L. Wang, J. Wang, F. Jia, C. Wang, M. Chen, Nanoporous carbon synthesized coal tar pitch and its capacitive performance. J. Mater. Chem. A **1**, 9498–9507 (2013). https://doi.org/10.1039/C3TA10426E
44. H. Lin, D. Chen, H. Liu, X. Zou, T. Chen, Effect of MnO_2 crystalline structure on the catalytic oxidation of formaldehyde. Aerosol Air Qual. Res. **17**, 1011–1020 (2017). https://doi.org/10.4209/aaqr.2017.01.0013
45. L. Li, C. Nan, J. Lu, Q. Peng, Y. Li, Nanotube α-MnO_2: High surface area and enhanced lithium battery properties. Chem. Commun. **48**, 6945–6947 (2012). https://doi.org/10.1039/C2CC32306K
46. Y. Zhao, J. Misch, C.-A. Wang, Facile synthesis and characterization of MnO_2 nanomaterials as supercapacitor electrode materials. J. Mater. Sci. -Mater. Electron. **27**, 5533–5542 (2016). https://doi.org/10.1007/s10854-016-4457-x
47. P.F. Smith, B.J. Deibert, S. Kaushik, G. Gardner, S. Hwang, H. Wang, J.F. Al-Sharab, E. Garfunkel, L. Fabris, J. Li, G.C. Dismukes, Coordination geometry and oxidation state requirements of corner-sharing MnO_6 octahedra for water oxidation catalysis: An investigation of manganite (γ-MnOOH). Catalysis **6**, 2089–2099 (2016). https://doi.org/10.1021/acscatal.6b00099
48. E. Saputra, S. Muhammad, H. Sun, H.M. Ang, M.O. Tadé, S. Wang, Different crystallographic one-dimensional MnO_2 nanomaterials and their superior performance in catalytic phenol degradation. Environ. Sci. Technol. **47**, 5882–5887 (2013). https://doi.org/10.1021/es400878c
49. Y. Peng, H. Chang, Y. Dai, J. Li, Structural and surface effect of MnO_2 for low temperature selective catalytic reduction of NO with NH_3. Procedia Environ. **18**, 384–390 (2013). https://doi.org/10.1016/j.proenv.2013.04.051
50. H. Ying-Ying, W. Zhao-Yin, J. Jun, Rapid low-cost synthesis and enhanced electrochemical properties of mesoporous Mn_3O_4 nanorods. J. Inorg. Mater. **28**(9), 1045–1050 (2013). https://doi.org/10.3724/SP.J.1077.2013.13146
51. X. Li, T. Fan, Z. Liu, J. Ding, Q. Guo, D. Zhang, Synthesis and hierarchical pore structure of biomorphic manganese oxide derived from woods. J. Eur. Ceram. Soc. **26**, 3657–3664 (2006). https://doi.org/10.1016/j.jeurceramsoc.2005.10.015
52. S. Saha, A. Pal, Microporous assembly of MnO_2 nanosheets for malachite green degradation. Sep. Purif. Technol. **134**, 26–36 (2014). https://doi.org/10.1016/j.seppur.2014.07.021
53. L.-T. Tseng, Y. Lu, H.M. Fan, Y. Wang, X. Liu, P. Munroe, S. Li, J. Yi, Magnetic properties in α-MnO_2 doped with alkaline elements. Sci. Rep. **5**, 9094 (2015). https://doi.org/10.1038/srep09094
54. J. Qu, L. Shi, C. He, F. Gao, B. Li, Q. Zhou, H. Hu, G. Shao, X. Wang, J. Qui, Highly efficient synthesis of graphene/MnO_2 hybrids and their application for ultrafast oxidative decomposition of methylene blue. Carbon **66**, 485–492 (2014). https://doi.org/10.1016/j.carbon.2013.09.025
55. T. Uematsu, Y. Miyamoto, Y. Ogasawara, K. Suzuki, K. Yamaguchi, N. Mizuno, Molybdenum-doped α-MnO_2 as an efficient reusable heterogeneous catalyst for aerobic sulfide oxygenation.

Catal. Sci. Technol. **6**, 222–233 (2016). https://doi.org/10.1039/C5CY01552A

56. C. Liu, D. Pan, X. Tang, M. Hou, Q. Zhou, J. Zhou, Degradation of Rhodamine B by the α-MnO_2/peroxymonosulfate system. Water Air Soil Pollut. **227**(92), 1–10 (2016). https://doi.org/10.1007/s11270-016-2782-6
57. N.A. Fathy, S.E. El-Shafey, O.I. El-Shafey, W.S. Mohamed, Oxidative degradation of RB19 dye by a novel γ-MnO_2/MWCNT nanocomposite catalyst with H_2O_2. J. Environ. Chem. Eng. **1**(4), 858–864 (2013). https://doi.org/10.1016/j.jece.2013.07.028
58. C.M. Cellier, V. Vromman, V. Ruaux, E.M. Gaigneaux, P. Grange, Sulfation mechanism and catalytic behavior of manganese oxide in the oxidation of methanetiol. J. Phys. Chem. B **108**, 9989–10001 (2004). https://doi.org/10.1021/jp049158m
59. C. Cellier, S. Lambert, E.M. Gaigneaux, C. Poleunis, V. Ruaux, P. Eloy, C. Lahousse, P. Bertrand, J.-P. Pirard, P. Grange, Investigation of the preparation an activity of gold catalyst in the total oxidation of n-hexane. Appl. Catal., B (2007). https://doi.org/10.1016/J.APCATB.2006.01.026
60. C. Liu, J. Wang, L. Xiang, Synthesis and surface characterization of γ-MnO_2 nanostructures. J. Nanomater. **4**, 389634 (2013). https://doi.org/10.1155/2013/389634
61. F.A. Caliman, L.C. Apostol, D. Bulgariu, L. Bulgariu, M. Gavrilescu, Study regarding the sorption of erythrosine from aqueous solution onto soil. Environ. Eng. Manag. J. (2009). https://doi.org/10.30638/eemj.2009.196